

## First Flight Results of the MOVE-II Satellite

Sebastian Rückerl, David Meßmann, Nicolas Appel, Jonis Kiesbye,  
 Florian Schummer, Markus Fähling, Lucas Krempel, Tejas Kale, Alexander Lill,  
 Gonzalo Reina, Patrick Schnierle, Sebastian Würhl, Martin Langer

Institute of Astronautics, Technical University of Munich  
 85748 Garching, Germany; +49 (0)89/289-16014  
 s.rueckerl@tum.de

Martin Lülf

Institute for Communications and Navigation, Technical University of Munich  
 80333 Munich, Germany

### ABSTRACT

MOVE-II (Munich Orbital Verification Experiment) is the second satellite of the Technical University of Munich's educational CubeSat program. On December 3, 2018, the satellite was launched on the SSO-A SmallSat Express from the Vandenberg Air Force Base. The following paper shows on-orbit results of the first eight months of operations. It includes analyses based on our own data as well as the open-source ground station network SatNOGS. Lessons learned from mission operations and recommendations for future educational missions are provided. The technical goals of the mission are verifying the satellite's bus and the qualification of a novel type of quadro-junction solar cells. Over 200 students have been developing and testing all components of the satellite since the beginning of the project in April 2015. During the course of the project, the students designed all necessary technology for a CubeSat bus, with the exception of the electrical power system and the on-board computer's hardware. Furthermore, the students developed ground station software as well as an operations interface from scratch. The technological achievements of the mission range from a linux-based onboard computer software over a magnetorquer-based attitude determination and control system to two novel transceivers for UHF/VHF and S-Band. A reusable mechanism, based on shape-memory-alloys, deployed the four solar panels, providing the necessary power. Only hours after the deployment, we received the first signals of the satellite. The commissioning of the ground station and the effects of an insufficient power budget of the tumbling satellite preoccupied us during the first month, as well as frequent watchdog resets. During the commissioning of the Attitude Determination and Control System (ADCS), a spin rate of  $200^{\circ}/s$  was observed, although the actuators were not activated yet. Detailed analysis with the help of recordings provided by our own ground station as well as the SatNOGS ground station network revealed a slow increase of the spin rate since the launch. In the following weeks the spin rate further increased to over  $500^{\circ}/s$ . Afterwards we were able to modify our ADCS actuation in a way to reduce the spin rate again. Currently MOVE-II is detumbled and we are moving towards regular scientific operation.

After a presentation of the results, lessons learned from our mission operations are discussed. The paper discusses the measured values and analyzes the reasons for the observed behaviour. Also the changes made on MOVE-IIb, a slightly improved copy of MOVE-II, will be explained. The paper concludes with recommendations for designers of upcoming educational satellite missions, especially regarding resilience against negative power budgets.

### INTRODUCTION

In 2006 the development of CubeSats at the Technical University of Munich (TUM) began with the first satellite of the Munich Orbital Verification Experiment (MOVE) called First-MOVE [1]. Members of the Institute of Astronautics (LRT) built most parts of this satellite. First-MOVE was launched into low earth orbit in November 2013 from Yasny.

The development of MOVE-II, the successor of First-MOVE began in 2015. This satellite was developed and built by an interdisciplinary team of over 200 students

under supervision of the LRT. The development process of MOVE-II was highly influenced by the lessons learned of First-MOVE [2]. This leads to a design with strong requirements for testability, reliability and performance [3, 4]. MOVE-II was launched into a sun-synchronous orbit on December 3rd on-board the SSO-A launch, and is since then operated by students in cooperation with the LRT.

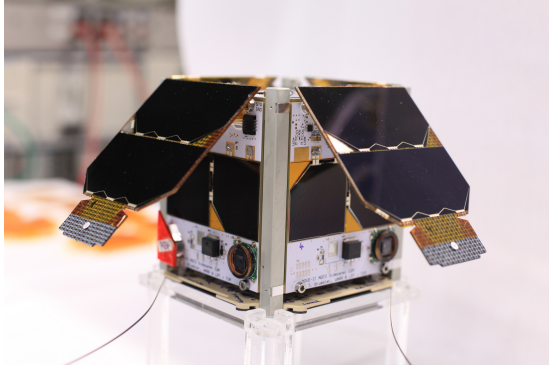


**Figure 1: Fully integrated MOVE-II satellite before shipment**

## THE MOVE-II SATELLITE

The MOVE-II satellite (see figure 1) is split up into smaller subsystems. In this part the main developments will be presented.

### CDH

The Command and Data Handling (CDH) system is the board computer of the CubeSat. It is connected to all other subsystems. It handles communication between the subsystems, storage of configuration and housekeeping data, and commanding of the satellite. Also, the CDH can either manually or automatically set the operation mode of the whole system.

#### Hardware

The CDH hardware is a stack of three boards. First, the carrier board is part of the satellite structure and is connected to the PC/104 bus. Second, a processing module is attached to the carrier board. Finally, a storage module is stacked on top of the processing module.

The carrier board provides a GPS module, a Ferroelectric Random Access Memory (FRAM), and a microcontroller serving as a watchdog. The processing module consists of a SAMA5D2 processor, a Random Access Memory (RAM) and NAND flash storage. The storage module provides an additional SpaceVault flash storage and two micro-SD card readers. The specifications can be found in Table 1.

**Table 1: CDH Hardware Specification**

Component	Specification
Power Supply	5 V
Clock Frequency	400 MHz
RAM Size	512 MB
NAND Storage	512 MB
FRAM Storage	32 kB
SpaceVault	1.5 GB

#### Flash Layout and Boot

The NAND flash of the CDH board is divided in multiple blocks. One block contains U-Boot, the boot

loader. Three blocks redundantly contain linux kernels with an integrated rescue system, which is described as “rawRESQ mode“ below. Another three blocks store the system images. A system image contains all userspace programs and default configurations. The FRAM stores two types of values. First, it stores state variables needed for communication with the groundstation when using the rescue system. Second, it contains information about the system images. The information is the time the image was last booted and the uptime of the image. When booting the CDH board U-Boot is started first. U-Boot then randomly chooses one of the kernels. If the kernel fails to load, the system will reboot until a working kernel is chosen. The rescue system will then load the image variables from the FRAM. Images that last had an uptime under 10 minutes will be discarded for boot. If all images are discarded, the satellite will stay in rawRESQ mode.

#### Software Components

The system image of the satellite consists of various services running in the background, called daemons. The daemons and their connections can be seen in figure 2. There is one daemon for each subsystem and daemons that control the state of the satellite, or collect data to send to the ground. As not all subsystems are connected to each other via a data link, the subsystems communicate with their respective daemon in the CDH, which in turn communicates with the other subsystems. The daemons are connected with each other using a software bus (D-Bus). The health monitoring system (HORST) of the satellite is also implemented as a daemon. HORST will receive sensor values from the other daemons via D-Bus and change modes if required. Another component is the Beacon Data Collector which constantly collects relevant data and sends it to the ground.

The satellite can be in different modes that define the behavior and current capabilities of the satellite. The various subsystems of the satellite can be on, off or sleeping depending on the mode.

#### rawRESQ mode

When booting the satellite the kernel will load a minimal set of programs and services to operate the satellite. This set is called rawRESQ. When all system images fail to load the satellite will stay in this mode. The mission control team is still able to contact and operate the satellite in this mode. Most subsystems are either disabled or run with less functionality. RawRESQ is used to analyze problems and repair the satellite if necessary. Once the recovery is completed the system images will be flagged as bootable and the nominal system can be started.

#### LEOP

Launch and Early Operations (LEOP) is the configuration the satellite is in after first deploying the satellite in space. After 30 min the deployment mechanism of the Flappannels and antennas will be activated and triggered

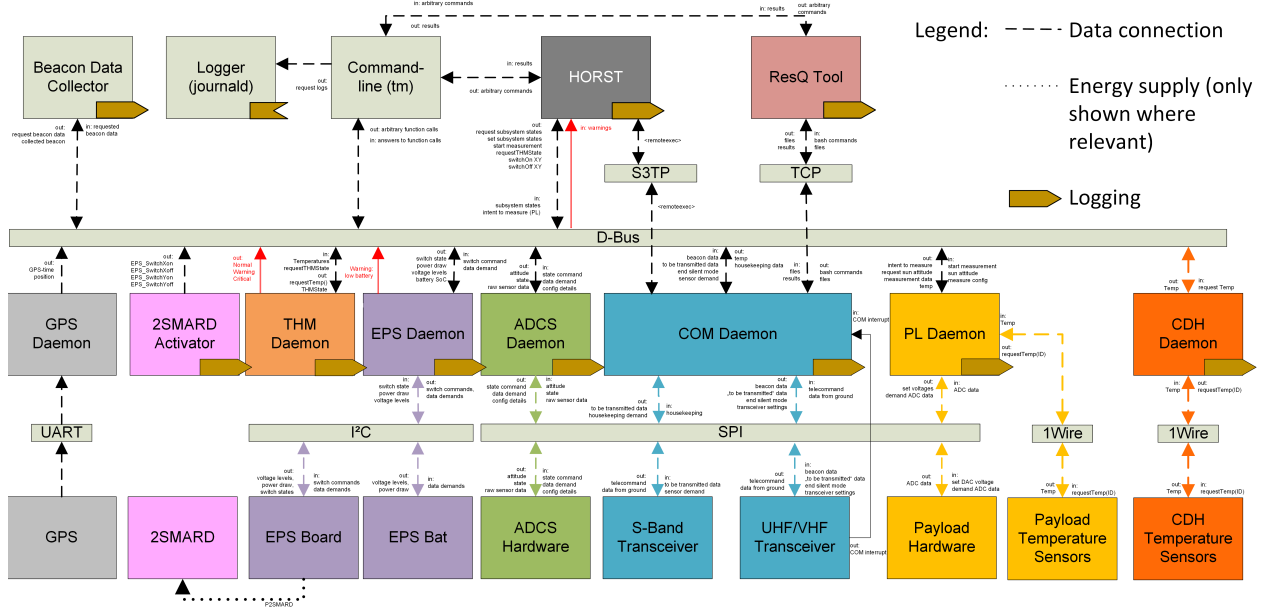


Figure 2: MOVE-II Software Architecture

regularly. 15 min after deployment of the antennas the satellite will also end its radio silent phase. Due to these activations the satellite will consume more power than it generates in this state. All other subsystems are disabled in LEOP.

#### SCIOPS

The satellite can be set into Science Operations (SCIOPS) manually from the ground. In this mode the satellite will try to automatically point to the sun using the attitude determination and control system (ADCS) and perform payload (PL) measurements. If the satellite is not in safemode all subsystems are enabled.

#### Safemode

The satellite is in safemode if HORST detects high temperatures or low battery. In safemode Payload, ADCS, GPS and S-Band are disabled. Also the CDH is only awake for 10 s every minute and suspended for the remaining 50 s (called sleepwake), and the ADCS is set into sleep mode.

#### Manualmode

In the nominal state of the system, HORST will decide which modes of the satellite to enter. If the mission control team needs the satellite to be in different modes, manualmode can be enabled. In this mode HORST will not perform any actions for 30 minutes.

#### Maneuvermode

If the ADCS of the satellite is enabled HORST will automatically enable its sun pointing mode. If the mission control team wants to set it to another mode maneuvermode can be enabled. The system will stay in this mode until rebooting.

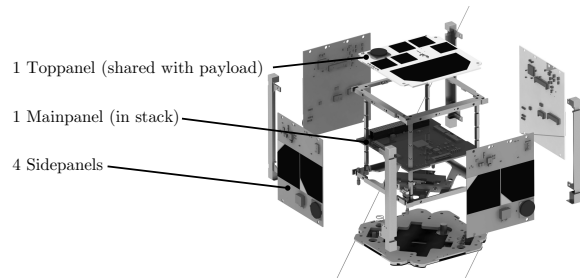


Figure 3: Overview of the ADCS hardware boards [5]

#### ADCS

The ADCS of MOVE-II uses active magnetorquer control to achieve its two main control strategies: Detumbling and sun pointing. It is a self-developed system with printed circuit board (PCB) integrated magnetorquer coils and commercial off-the-shelf (COTS) sensors. Physically, the ADCS consists of a Mainpanel located in the center of the stack and five outer panels: the so-called Sidepanels and the Toppanel. The arrangement of these boards are depicted in figure 3.

The Sidepanels share space with the solar cells on the sides and the Payload on the Top. Each ADCS panel features a magnetorquer, coil driver electronics, a gyroscope, a magnetometer, a sun sensor (excluding the Mainpanel) and a microcontroller.

The Sidepanel microcontrollers receive commands from the Mainpanel over a Serial Peripheral Interface (SPI). They handle magnetorquer control, sensor interfacing,

sensor calibration and preprocessing. The Mainpanel microcontroller is responsible for the attitude determination and attitude control calculations using sensor data gathered from the Sidepanels. It also commands the Sidepanels to actuate their magnetorquers. Additionally, it handles commands and configuration received from the CDH and responds with housekeeping and other sensor data [5].

A simple and robust B-Dot control strategy is implemented for dampening the initial satellite spin after deployment. For scientific operations, a linear model-based control strategy is used to point the Toppanel towards the sun, ensuring adequate power generation [6]. An Extended Kalman filter is applied for attitude estimation [5].

The six available magnetorquers can be used in either a single or dual magnetorquer per axis configuration. Additionally only one of the six available gyroscopes or magnetometers is required for ADCS operation. The active magnetorquers and sensors can be configured from ground, and are thus adding redundancy to the system. All ADCS microcontrollers can be flashed by the CDH allowing for in-orbit software updates or flash corruption recovery.

### COM

The communication (COM) subsystem consists of two transceivers for low and high data rate services. Low data rate services, such as telemetry and telecommand, are provided by the UHF/VHF transceiver (see fig. 4). An additional S-Band transceiver can provide high data rates of 3 MBit/s. Due to the high spinning rate of the satellite, the operation of the S-Band transceiver could not be verified at this point. The following will therefore concentrate on the UHF/VHF subsystem. An overview of the RF parameters is given in table 2.

The UHF/VHF transceiver uses a custom RF design with discrete IC components for frequency synthesis, mixing and D/A and A/D conversion. All VHF transmitter components can be switched off or set to sleep, which provides significant power savings. This was done as the device needs to be very power saving, reliable and also to keep the design modular.

After the analog RF path and digitizing, all further processing is performed in an FPGA. The FPGA used in the design is a Xilinx Spartan 6 LX45. The Spartan 6 series was chosen since it is reported to be sufficiently radiation tolerant but also because it can be programmed with a free Xilinx ISE license. To prevent bit flips in the FPGA configuration memory, inherently radiation tolerant magnetoresistive RAM (MRAM) is used.

Both up- and downlink use a phase-shift-keying (PSK) modulation type. The downlink implements several variants of 2-ary (BPSK) and 4-ary (QPSK) PSK and



**Figure 4: Pictures of the UHF/VHF Flight Model**

Property	Value
Downlink Frequency	145.94 MHz
Downlink Bandwidth	18.75 kHz
Downlink RF Power	27 dBm
Downlink Modulation	BPSK/QPSK
Downlink Symbol Rate	12.5 kBaud
Downlink Coding	LDPC 1/2, 4/5
Uplink Frequency	437.8 MHz
Uplink Bandwidth	18.75 kHz
Uplink Modulation	DBPSK
Uplink Symbol Rate	12.5 kBaud

**Table 2: UHF/VHF Transceiver Parameters**

offset-QQPSK (OQPSK). This gives the operators more control over the radio link and allows higher data rates if needed.

During the LEOP phase, only the downlink used BPSK together with a (2048, 1024) AR4JA LDPC code [7] because of its higher robustness. These codes provide very high performance, but decoding is too complex to use them on the uplink. The uplink uses differential encoded BPSK (DBPSK), which significantly reduces receiver complexity at the expense of slightly increased BER.

In the main mission phase, the higher order QPSK and OQPSK modulations will be used together with a (5120, 4096) AR4JA LDPC code. Modulation and coding can be separately chosen by the operator. The maximum possible data rate of the system is 20 kBit/s.

The data link layer protocol used on the radio links is Nanolink [8]. Nanolink is a reliable, connection oriented, packet based protocol for CubeSats and other spaceborne assets with similar bandwidth and hardware resources. It is designed for asymmetric links with small bandwidth-delay product. The protocol operates efficiently and

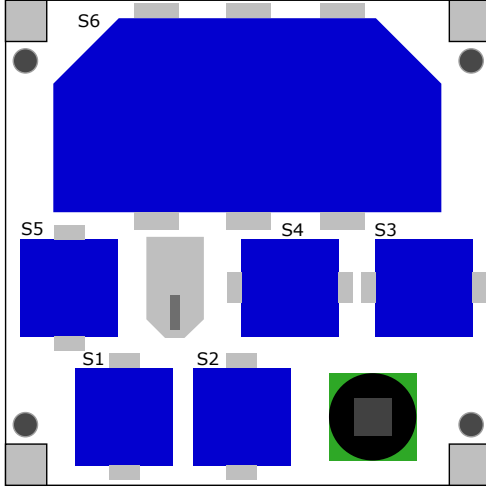


**Figure 5:** MOVE-II PL panel with one four junction solar cell and the corresponding single junction cells

reliably in moderate signal quality due to a type-I hybrid selective acknowledge automatic repeat request (ARQ) scheme. Extensible header structures reduce the required overhead, especially with regard to the ARQ return channel.

A more detailed description of the COM Subsystems can be found in [9].

### PL

The payload (PL) of MOVE-II characterizes novel four junction solar cells in space conditions. It is not possible to obtain similar data on ground, as state of the art air mass zero (AM0) sun simulators are not able to reproduce the full solar spectrum in detail. Furthermore, other influences such as thermal cycling and cosmic ray impacts can not be simulated at the same time. Thus, the PL will give an insight in the performance of the novel four junction cells in realistic space conditions [10].

The PL is located on the topmost panel of the CubeSat. This ensures optimal sun illumination conditions with the satellite in sun pointing mode. The PL carries one four junction solar cell and additionally the corresponding single junction cells. Furthermore, one cell is added without a cover glass. As the cell is lacking a protective cover, it will undergo an accelerated degradation and enables the prediction of the performance for protected solar cells in a long-term mission. As the parameters of the solar cells vary with temperature, each cell has a temperature sensor attached on the back-side of the PL panel. Additionally, the sun angle is evaluated by a dedicated sensor on the same panel. An overview of the PL panel with all six solar cells is depicted in figure 5. The electrical characterization is done with a sweep through the current versus voltage (I-V) curve from open circuit voltage to short circuit current of the solar cell. For

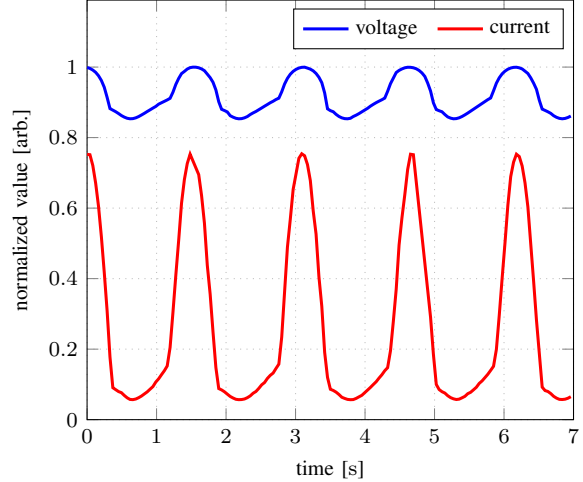


**Figure 6:** Normalized open circuit voltage and short circuit current measurements taken by the PL during the rotation of the CubeSat

the sweep a controllable load is connected to each cell and high-resolution analog to digital converters (ADC's) measure continuously voltage and current data points. To ensure the functionality of the PL in space environment, the key components were selected by reviewing publicly available radiation test data. Additionally, a hardware self-test is implemented to do in orbit accuracy checks of the PL.

Before the CubeSat was sent into space, the PL was tested in functionality and measurement accuracy on ground. The absolute accuracy of current and voltage measurement was evaluated with a calibrated Keithley 2400 sourcemeter. The results of this tests yield a maximum deviation in current measurement of 0.6 % and for the voltage measurement only 0.04 %. Further tests included direct comparison of I-V measurements to the standard method. As already mentioned, a hardware self-test is included to determine any changes in the measurement accuracy.

The PL is already active but due to the high rotational rates, no full I-V curve could be measured until now. The status of the PL was evaluated by executing the hardware self-test which did not show any deviations in the measurement accuracy. To do a functionality test, the PL was switched to a specific mode, where it measures continuously open circuit or short circuit currents of the solar cells. The data received from these measurements were as expected. Due to the rotation of the satellite the short circuit current is changing rapidly over time as it is directly correlated with the incoming solar radiation. The open circuit voltage is only decreasing 15 % from high to low illumination. A graph of measurements taken by the PL during the rotation can be seen in figure 6.

## MOVE-II GROUND SEGMENT

### *Ground Station*

The primary ground station for the TM/TC link is a ham radio station located on the roof of the LRT. The antennas for the up- and downlink are mounted onto a COTS component 2-axis rotator that points the antenna towards the computed satellite position based on the two line element (TLE) file for the satellite. The VHF antenna is connected to a COTS low noise amplifier (LNA) that is mounted onto the rotator and from there on it connects to a software defined radio (SDR). For the uplink the samples are sent to a SDR which is connected to a high power amplifier which is capable of providing enough power to reach the maximum allowed transmission power in the amateur UHF band of 750 W PEP. Previous satellite missions have found that there are a lot of terrestrial radio sources –especially over western Europe– that interfere with the uplink signals[11]. Since our ground station is located in western Europe the high output power capability of our groundstation allows us to reliably reach the satellite even in the presence of strong interference from other terrestrial sources.

The (de)modulation and en-/decoding of the signal is performed in software. For the downlink we use a GNURadio flowgraph with custom blocks. For the uplink we started with GNURadio as well but had to fight growing latency and head of line blocking, so we switched to a custom made software. Both the uplink and downlink compensate the frequency shift caused by the Doppler effect based on computed satellite position and velocity from TLE orbits.

### *Operations Interface*

The MOVE-II Operations Interface can be split up into two major parts: the backend and the frontend components.

The backend is responsible for parsing, storing and providing the beacon, telemetry and housekeeping data received from the satellite. It also acts as the counterpart of the commanding interface on the satellite by implementing our custom commanding protocol RESQ. This is combined with a commanding queue and a logging component that allows us to reproduce the exact command sequence that was executed on the satellite and prepare the command sequence for upcoming overpasses. All these services are provided to any frontend or automation implementation via a representational state transfer (REST) application programming interface (API) in combination with a WebSocket interface to update the user interface whenever new data is available.

The frontend of the Operations Interface is a web based graphical user interface that provides overview and general monitoring functionality combined with a user

configurable data analysis tool. This way all the data can be easily accessed and analyzed from any location using a browser. Besides the data analysis the frontend also abstracts the RESQ protocol from the user allowing for simpler commanding of the satellite.

## LAUNCH AND EARLY OPERATIONS

The commissioning of MOVE-II began with confirming that the deployment of our solar panels was successful. This was confirmed on June 4th, 01:30 UTC by observations of a SatNOGS groundstation in Australia [12]. We observed that the satellite was regularly sending a carrier-only signal and morse callsign, and thus the antennas must have deployed. In the following days, this was confirmed by received telemetry data from the electrical power system (EPS) showing that our solar cells were deployed.

### *TLE Detection*

The main challenge during the first overpasses was the accuracy of the provided TLE files, which at first was an estimate based on the position of the deployer rather than our satellite. An inaccurate TLE can lead to (1) a shift in contact times, resulting in incorrect antenna pointing and (2) an erroneous Doppler correction that will shift the downlink signal out of the matched filter. Both issues can cause a loss of communication with the satellite.

To mitigate these issues we simulated orbits that were shifted locations of the deployer on the orbital plane and prepared look-up tables for azimuth and elevation angles based on these simulations. We pointed the antennas ahead of time towards the position where the satellite was expected to rise and waited for the satellite signal to appear in the waterfall diagram. By observing the actual time of acquisition of signal (AOS) we could identify the simulated situation that best matched our observation. We could then use the angles in the corresponding look-up table to move the antennas by hand during the first overpass. The automatic Doppler correction was disabled during the first overpasses and instead the operator could manually adjust the frequency offset using a slider in GNURadio. In addition, the original baseband signal was recorded and was replayed with an automatic Doppler correction once the correct orbital parameters were obtained.

This procedure together with the special signal structure allowed us to identify the downlink signal of MOVE-II in the waterfall and to obtain a first set of orbital parameters during the first overpass.

In the following overpasses North American Aerospace Defense Command (NORAD) continuously added new objects to the TLE database and the elements of the existing objects became more precise due to longer observation times. Rather than further varying the provided

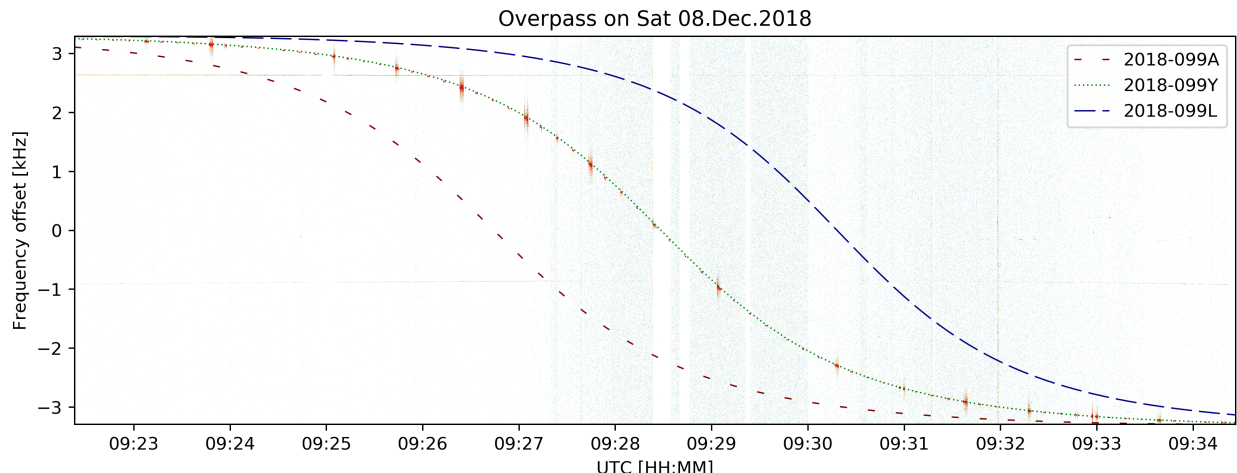


**Figure 7: Recorded waterfall of the MOVE-II satellite on the 8th of December 2018 overlaid with the computed Doppler shifts from three different TLE objects.**

orbital parameters we could now identify which of the TLE objects belonged to MOVE-II. This was achieved by comparing the observed Doppler shift with the predicted Doppler shifts from the various TLE objects. Figure 7 shows the recorded waterfall of the overpass on the 8th of December 2018 as well as the predicted Doppler shifts for the objects 2018-099A, 2018-099Y and 2018-099L. Today these objects have been identified as MINXSS-2, MOVE-II and AISTECHSAT 2, respectively. With time the objects drifted further apart. Each consecutive overpass there where more objects that could be excluded from the list of MOVE-II candidates. This analysis was supported by booking overpasses of the TLE candidates on several SatNOGS ground stations. The agreement of the MOVE-II signal with the booked TLE data set could be judged by looking at the frequency residual in the Doppler corrected waterfall graphs that SatNOGS provided. This allowed us to observe and match MOVE-II orbits at locations around the world. Finally only object 2018-099Y (NORAD catalog number 43780) continued to provide a consistent match between the predicted and observed Doppler shifts and thus the TLE of MOVE-II had been identified.

#### ***Commissioning of Subsystems and Early Operations***

The next step in the commissioning procedure was to deactivate the deployment mechanism. However, we faced a few problems while trying to do this. First, our power budget was slightly negative. The battery was drained after two days. As a consequence, the satellite was switched off in eclipse regularly. This also switches off the battery heater, leading to temperatures down to  $-5^{\circ}\text{C}$  in the core of the satellite. Afterwards we observed several CDH freezes, most likely due to some poorly understood conditions resulting from the cold temperatures. This

triggered EPS watchdog resets, causing us to go into the rawRESQ mode. Unfortunately even more watchdog resets were observed in rawRESQ.

A further problem was that our COM link was not nearly as stable as anticipated, most likely due to the high spin rates of the satellite. Thus we had to command our satellite without a stable link. This was achieved by sending commands up repeatedly at a high frequency until we got confirmation that the command was executed. One major issue was that the command ID needs to be increased by one for each subsequent command, otherwise the command is dropped by the satellite. The problem here was that there is no direct way to find out this ID without a stable link. Therefore we had to purposely change some telemetry values in the beacon with each command in order to confirm that the command was received. This way we could keep track of the required ID. Because of some issues with this commanding scheme (which was neither intended nor tested), it took us until the 21st of January to deactivate our deployment mechanism.

Normally we would then proceed with testing each subsystem before going into SCIOPS, which turns on our ADCS. However, because of the power budget problems and because, at this point in time, we also noticed through the signal fading that the satellite was turning quite fast, we prioritized commissioning the ADCS. We first enabled only the sensors on the 23rd of January, which showed that we were turning at  $201^{\circ}/\text{s}$ . One week later, on the 30th of January, we enabled the ADCS with the actuators for the first time.

To verify the functionality of the payload measurement device, we triggered some measurements. The first measurements were performed on 7th of May. This

data showed that the PL hardware was still working as expected, although the data could not be used for the intended scientific purposes because of a huge pointing error and uncertainty due to the high spin rate.

## FAST SPINNING MOVE

### Hypothesis

Several causes have been considered to explain the increasing angular velocity of the satellite. The current theory suggests electro-magnetic disturbance torques caused by other subsystems. The most likely candidates are the COM transceiver, the EPS and the solar cell wiring of the Side- and Flappanel. From flight model testing at an external facility, we know that the COM transceiver and the EPS board indeed produce a dipole moment that induces a magnetic disturbance torque on the satellite. Since the dipole moment of the COM transceiver is not modulated depending on the attitude of the satellite, we assume its net effect on the momentum of the satellite to be zero. The maximum power point trackers of the EPS however modulate their dipole moment depending on the solar array currents which vary based on the satellite's attitude towards the sun. So the EPS is a possible motor that might have contributed to speed up the satellite. Since we neither have the appropriate test setup for further analysis nor know the proprietary schematics and board layout of the EPS, we could not assess the effect that our EPS has on the satellite's velocity so far.

A closer look on the Flappanel has revealed that the solar cell wiring forms a single-winded coil with an area of  $0.0018 \text{ m}^2$  and a maximum current of  $0.45 \text{ A}$ . The current path and the resulting dipole moment (green arrow) are visualized in figure 8 for a single Flappanel. The magnitude of the dipole depends on the solar incidence angle. Thus, no dipole moment is generated for an incident angle over  $90^\circ$ , nor in eclipse. Whenever the solar cells are illuminated, a torque perpendicular to the magnetic field of the Earth and the Flappanel dipole moment vectors is generated. The Flappanel dipole moments depend on the attitude of the satellite and can add angular momentum to or remove angular momentum from the satellite. We consider this theory the prime candidate for explaining MOVE-II's fast spinning motion. The Sidepanels also produce a small dipole moment due to their solar cell wiring. However, it is negligible compared to the Flappanel dipole.

In order to get a better understanding of this disturbance, several simulations of a spinning satellite without any actuation have been conducted. A model of the solar magnetic disturbance caused by the Flappanel solar cell wiring was integrated into the simulation. By also adding a constant residual dipole moment, we can see an increasing trend of the spin rate and a characteristic oscillation depicted in figure 9. A similar phenomenon

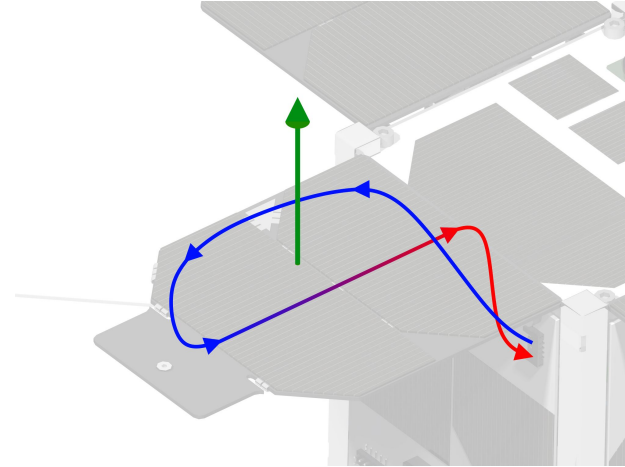


**Figure 8: Magnetic Dipole Moment induced by current flow of the solar cell wiring**

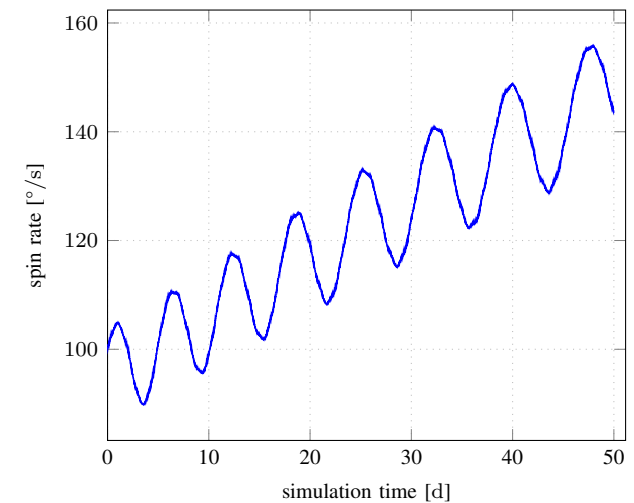


**Figure 9: Simulated solar magnetism disturbance**

as seen from the real data depicted in figure 11 could be reproduced. Although these first simulation results are plausible, we do not fully understand the complete phenomenon that causes the characteristic curve yet. Further investigations are planned in the future.

### Attitude Control Strategy

The ADCS has been designed to reliably work for rotational speeds up to approximately  $20^\circ/\text{s}$ . For very high angular rates, the timings of the implementation will strongly affect the control performance. We distinguish three different effects on the control performance:

1. Length of the actuation interval: For both detumbling and sun pointing the coils are actuated for a specified amount of time with a constant current. If the actuation time equals the revolution time of the satellite, there will be no net-torque. This effect is

- periodic with the angular velocity and influences the efficiency of the controller.
2. Time between sensor measurement and actuation: This shifts the actuation period to a moment in time after the actual measurement. The time difference with the angular velocity translates to an angle shift of the controller. Every  $180^\circ$  the actuation direction of the controller will invert and so determine if the satellite accelerates or decelerates. Between those, there are boundary regions where the controller is unstable.
  3. Sensor measurement buffering: A buffer for magnetometer measurements to compute the time derivative of the magnetic field ( $B$ -dot) is implemented. If the satellite rotates too much in this time period, the derivative can not be considered linear anymore.

The overall stability regions result from all effects explained above. In order to determine the location of these stability regions, several simulations, calculations and hardware tests have been done. The plot in figure 10 illustrates the stability regions determined from several simulation test runs. In each simulation the initial spin rate, which is shown on the x-axis of the plot, is varied. The angular rate difference after the simulation has ended, is given on the y-axis. A controller in the red domain will spin-up and in the green domain spin-down the satellite. The simulation results form curves which are characteristic for each controller. The curve for the state-feedback sun pointing controller is depicted in red, whereas the result for the  $B$ -dot detumbling controller is depicted in blue. For rotational velocities above  $10^\circ/\text{s}$ , the sun pointing controller behaves like a detumbling controller. Therefore, it can be also used to slow down the satellite and, since this controller has a different length of actuation interval, the stability regions differ from the actual detumbling controller. A software-in-the-loop simulation employing the space environment and sensor simulation from [13] produces the result that the first stability boundary for detumbling is at  $290^\circ/\text{s}$  and for sun pointing  $219.5^\circ/\text{s}$ . These simulated numbers are very close to theoretical calculations.

As the exact delays are not exactly known, the real stability boundaries may differ. In a real hardware test within a Helmholtz coil environment, the boundary is continuous as efficiency towards it decreases and noise becomes dominant. For the sun pointing controller, the upper limit where actuation can be seen is  $160^\circ/\text{s}$ . The lower limit of the inverse sun pointing controller is  $180^\circ/\text{s}$ . The boundary must be between those limits and is thus much lower than the simulated value of  $219.5^\circ/\text{s}$ . Also for the detumbling controller, the boundary is lower than the simulated value and efficiency decreases towards the detection limit already at around  $230^\circ/\text{s}$ .

In order to use controllers in the unstable regions, in

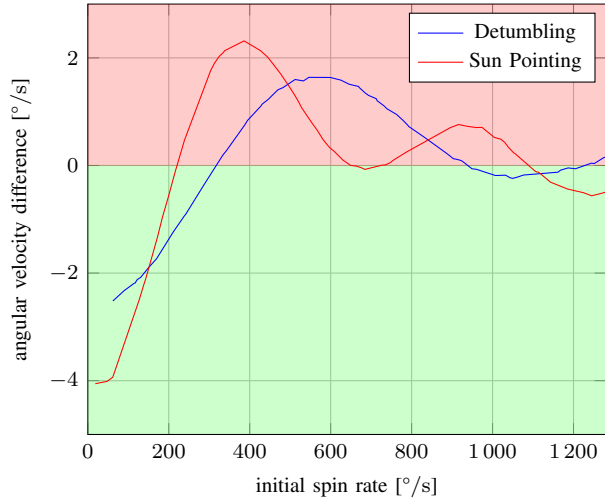


**Figure 10:** Results of simulation showing stability regions of the ADCS controllers. The green region indicates a stable controller, the red region an unstable controller.

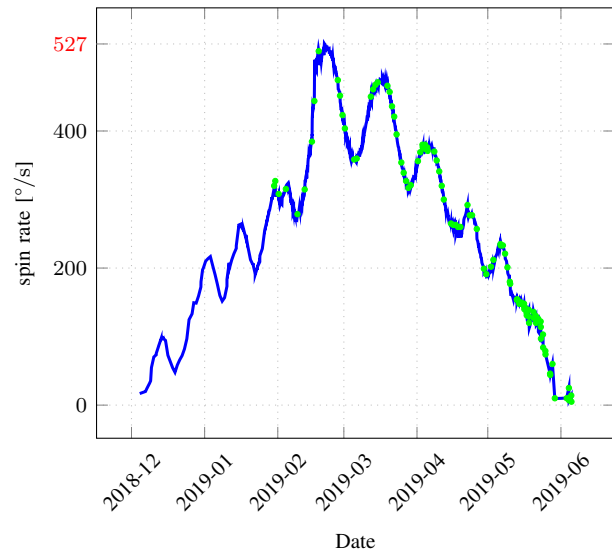


**Figure 11:** MOVE-II tumbling rate as estimated based on observed signal fading. Green dots indicate successful ADCS actuations

which the satellite would be normally accelerated, the sign of the controller gains can be inverted resulting in a  $180^\circ$  phase shift. With this change, the unstable regions become stable and vice versa. For practical reasons, we rather invert the sign of the magnetometer measurement, which is identical to inverting the sign of the controller gains for the applied control laws.

#### Detumbling success

MOVE-II only measures its spin-rate with the embedded sensors if ADCS is active. As ADCS was turned off for most of the time, we estimated the spin rate based

on the observed signal fading in the recorded signals. To get more data points, we combined our own data with the audio recordings generated for each overpass recorded with SatNOGS. More than 8000 overpasses for MOVE-II have been scheduled on SatNOGS so far [14]. Within each recording, we selected a part where several fading cycles could be observed and calculated the spin rate based on the average length of a cycle within one recording. Comparing the estimated spin rate to the norm of the angular velocities gathered by the ADCS sensors revealed an error of only a few °/s.

After initially getting aware of the high spin rate in January 2019, we did some first experimental ADCS actuations to gain knowledge on the behaviour of MOVE-II. This also included some actuations with incorrect controller settings, leading to an even further increased spin rate of MOVE-II to the overall maximal value of 527 °/s. End of February we finally managed to find a regular actuation sequence. This command was then executed once per day for about 3 months. In the early phase of the detumbling process a more frequent actuation pattern was not possible due to the limited power budget. Mid of May we were able to switch to a more frequent actuation scheme, leading to a faster decline of the spin rate. MOVE-II was finally detumbled (spin rate less than 10 °/s) on May 29th. Since that day we continue with the actuations to keep the spin rate low while also stabilizing the temperatures and the power budget of the satellite. Figure 11 depicts the observed spin rate of MOVE-II over the first 6 months in orbit, each green dot refers to one successful ADCS actuation.

## NEGATIVE POWER BUDGET

In this chapter we discuss the factors making MOVE-II's power budget negative and how we can still utilize the satellite effectively, which hopefully provides guidance to other teams on how to make their missions resilient against a negative power budget.

### Expectations

According to prior analyses, the power budget for MOVE-II was expected to be very tight before the satellite reaches its nominal sun pointing configuration. Depending on the temperature of the solar cells and the battery in orbit, as well as the tumbling mode, the budget was considered to just be sufficient or slightly too tight for a tumbling satellite in safe mode, i.e. all subsystems except for the UHF/VHF Transceiver, the CDH and the EPS are switched off [15, 13]. The reason for the tight margin are an oversized UHF/VHF transceiver consuming 1 W on average, a higher than expected EPS idle consumption of 0.65 W, and the CDH consuming an additional 0.23 W continuously.

During the launch and early operations phase, the shape

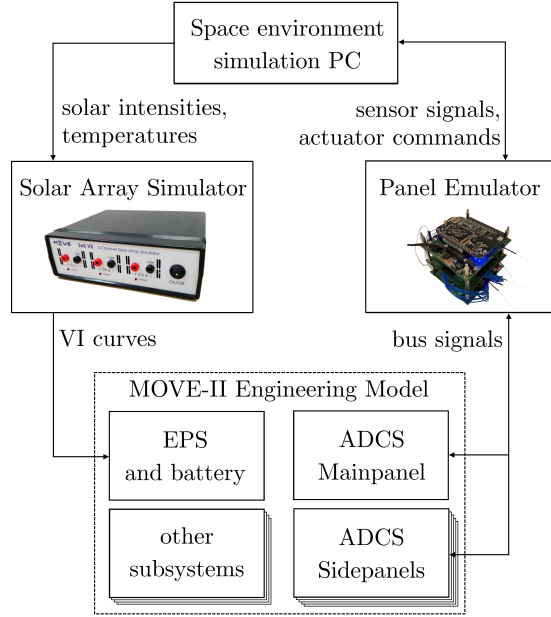


**Figure 12: Hardware-in-the-Loop setup for power budget verification of MOVE-II**

memory deployment mechanism consumes four 20 s long pulses of 11 W every three hours until receiving the deployment confirmation from ground. Due to this additional factor, the 20 W h battery of the satellite was expected to be drained over the course of the first days until successful two-way contact is established. Once the satellite is commissioned and points towards the sun, the power budget was expected to be more than sufficient.

### Verification

The ADCS simulation environment described in [16] was extended, so the solar irradiation of the satellite both with active and inactive ADCS could be studied in detail culminating in a Hardware in the Loop (HiL) simulation that could assess the performance of the maximum powerpoint trackers and all subsequent power conditioning circuitry of MOVE-II's EPS.

The solar array simulator described in [15] can simulate the realistic IV-curve of a solar array in real-time based on the solar irradiation and temperature of the array which the space environment simulation calculates. The whole engineering model of MOVE-II was embedded in a HiL setup shown in figure 12 where both the ADCS as well as the EPS received inputs from the space environment simulation. This HiL setup closely resembles the real power consumption of the satellite due to all subsystems being present and operating in flight configuration. Additionally, it allows us to assess the power generation depending on the ADCS sun pointing performance with a realistic simulation of the dynamics and disturbances in orbit.

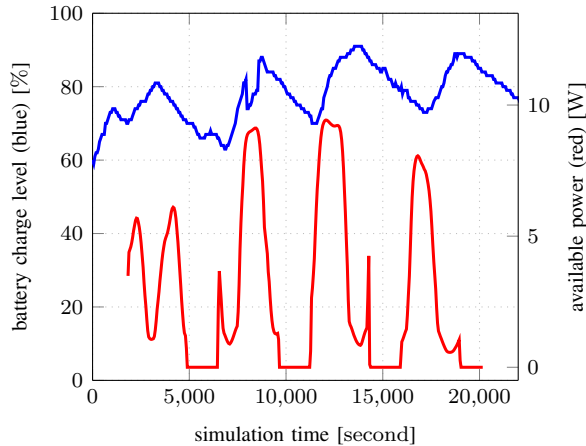


**Figure 13: Power budget verification using the HiL simulation in a tumbling scenario**

Two power budget test runs were executed with this setup covering the nominal SCIOPS phase with active sun pointing and the safe mode with only EPS, CDH, and the UHF/VHF transceiver turned on, while the satellite is freely tumbling at  $10^\circ/\text{s}$  [15]. These runs were executed at room temperature at which the battery had an internal resistance of  $0.42\ \Omega$  and its heater was turned off. While the SCIOPS phase clearly showed a positive power budget with a surplus energy of  $3\ \text{W h}$  per orbit, the safe mode simulation resulted in a slightly positive power budget indicating that every orbit generates a surplus of  $1\ \text{W h}$  or 5 % state-of-charge on average, shown in figure 13.

#### Preparations for a Resilient Power Budget

Not knowing if the satellite would stay power-positive during its flight, the under-voltage protection (UVP) of the satellite's battery was modified to ensure the satellite's proper restart in low-power conditions.

The UVP's original function is to protect the battery from deep-discharge. Once the UVP's trigger voltage  $U_{\text{trigger}}$  is reached, the UVP turns the whole satellite off. Only the maximum power point trackers remain connected to the battery for charging. After the UVP has triggered, it resets upon reaching the reset voltage  $U_{\text{res}}$ . In the original configuration,  $U_{\text{res}}$  was only slightly higher than  $U_{\text{trigger}}$ . Therefore the satellite would have turned on again with a nearly empty battery. Turning on so early bears the risk of ending up in a boot loop where the startup current of the satellite systems multiplied with the internal resistance of the battery drop the battery voltage below  $U_{\text{trigger}}$  and therefore prevent the satellite from reaching its ground station.

We modified  $U_{\text{res}}$  to  $8\ \text{V}$  instead of  $7\ \text{V}$ , while keeping  $U_{\text{trigger}}$  at the original value. According to our simulations and tests it should take several orbits for the satellite to reach the new  $U_{\text{res}}$ . Testing on ground showed that

we thereby should gain around  $2\ \text{W h}$  before the satellite switches on. This should be sufficient for multiple orbits. The battery's high internal resistance prevents charging the satellite even longer before reaching  $8\ \text{V}$ .

The modified UVP is designed to give us a few extra watt hours after draining the battery, so that we can operate the satellite for an orbit or more even if the power budget would be negative. The price that we pay for this extra energy are long phases in UVP shutdown where the UVP lets the satellite recharge and all its subsystems are completely turned off.

#### Flight Experience

Due to calibration issues with our ground station, the confirmation of successful deployment could not be sent, before the battery ran low for the first time.

MOVE-II's flight data clearly shows that the safe mode power budget is negative and the satellite usually turns off during eclipse. Several factors contributing to this behavior are listed below.

- Low temperature of the satellite
  - Battery heater consuming additional power
  - Increased battery resistance
- High power consumption of the essential subsystems
  - Oversized COM transceiver
  - High EPS idle consumption and misleading datasheet
- In-homogeneous solar cell placement

The temperature of the satellite is lower than anticipated. It was expected to tend towards the upper limit of the battery and therefore the team did not add multi-layer insulation to the battery. The minimum temperature of the satellite was simulated with the safe mode's heat dissipation of  $1.88\ \text{W}$  and not with the heat dissipation of the UVP shutdown, which is nearly zero. The safe mode was expected as power neutral, and therefore as a realistic cold case.

The low temperature results in the battery heater turning on during eclipse, creating an additional power draw of  $0.2\ \text{W}$  and thereby consuming about  $0.15\ \text{W h}$  of the  $1\ \text{W h}$  surplus measured during the verification run.

The effect of the cold battery on the power budget is expected to be even higher, although the team does not have a sufficient test setup for characterizing the battery at different temperatures. The internal resistance was measured to be  $0.42\ \Omega$  at room temperature which is a high value for lithium-polymer batteries and should rise significantly at temperatures of around  $0\ ^\circ\text{C}$ , which is the usual average for MOVE-II during most of its past flight. The EPS data that we could extract in May hints at an internal resistance of  $0.8\ \Omega$ . It is unclear to what extent the increase in battery resistance is attributed to the low temperature and to what extent we see degradation in

this number. A higher battery resistance results in higher losses while charging and discharging the battery.

The in-homogeneous placement of MOVE-II's solar cells also contributes to battery degradation. Figure 13 shows the available power from the solar arrays in red. Whenever the top of the satellite with the Flappanel is illuminated, the available power rises to almost 10 W, resulting in battery charge currents in excess of 1 A. Charging lithium batteries at temperatures below 0 °C is not recommended and should be limited to low currents to prevent degradation [17]. Since MOVE-II's EPS does not consider the battery temperature, it always charges at the maximum available current. The combination of MOVE-II's in-homogeneous solar cell distribution and its low temperature lead to degradation of its battery, a higher internal resistance, and to an even more negative power budget as long as the satellite stays in safe mode. The UVP only charges approximately one fourth of the 2 W h measured during ground testing due to the higher internal battery resistance. The result are shorter reset periods. Figure 14 shows the satellite in reset for one minute during an overpass which might be triggered by the UVP.

The problematic power situation described before provides a strong contrast to the successful commanding of the satellite and the detumbling maneuvers. The main reason that MOVE-II survives its negative safe mode power budget is the modified UVP described in the previous section. The main lessons that we learned from the mission so far and should be considered by future missions are:

- Make your power budget positive by a wide margin.
- Complement all values from datasheets regarding power consumption with your own measurements.
- Include a mechanism like the UVP that recharges the satellite for quite a long time after draining the battery. This element of circuitry saved the MOVE-II mission.
- Analyse the cold case scenario thoroughly. Is it possible that the satellite stays off for a longer time, creating a different cold case than the expected safe mode?

## IMPROVEMENTS ON MOVE-IIb

Within the last months we were building a second satellite, MOVE-IIb. MOVE-IIb is a copy of MOVE-II with only minor changes to mitigate the effects of a fast spinning satellite. MOVE-IIb is already integrated in the CubeSat deployer (see figure 15) and is awaiting its launch on a Soyuz rocket in July 2019. The following part will describe the changes made compared to MOVE-II.

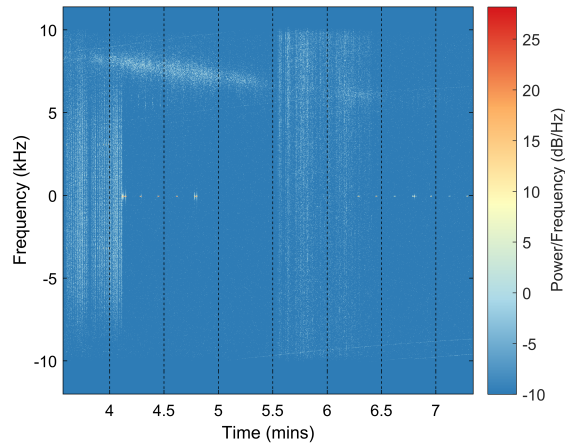


**Figure 14:** Overpass showing MOVE-II reboot due to UVP triggering. Shutdown happens 4.9 minutes into the overpass. Reboot at minute 6.



**Figure 15:** MOVE-IIb Satellite integrated in the EXO-LAUNCH CubeSat Deployer

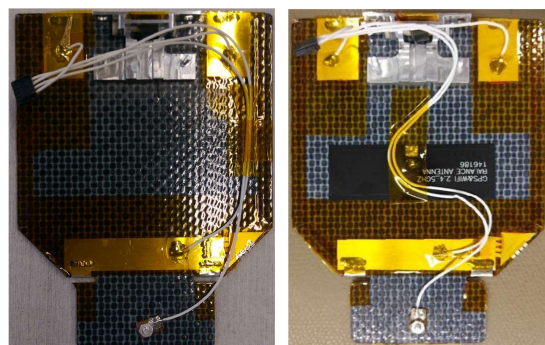


**Figure 16:** Solar cell wiring on the Flappanel of MOVE-II (left) and MOVE-IIb (right).

### Adjusted Solar Cell Wiring

The investigation process into the fast spin of MOVE-II overlapped the integration phase of MOVE-IIb so the PCB design could not be adjusted. Luckily, only the wiring of the Flappanel was identified as the main culprit of the spinning as pointed out in the "Fast Spinning MOVE" section. The kapton tape of MOVE-IIb's Flappanel was removed, the cable to the cathode of the solar cells bent in a shape where the generated dipoles will cancel each other out and the cable was secured with kapton tape again. A side-by-side comparison of the flight configuration of both MOVE-II's as well as MOVE-IIb's Flappanel is given in figure 16.

### ADCS Controller Countermeasures

The timing issues mentioned in the "Attitude Control Strategy" subsection can be avoided by modifications in the detumbling controller algorithm.

In order to compute the value of the time derivative of the magnetic field (B-dot), the kinematics of the satellite can be considered. Using a single measurement of the magnetic field, together with the angular velocity value measured by the gyroscopes, the magnetic field value can be extrapolated for a given time. By evaluating a simple vector kinematic equation with the extrapolated sensor data, the B-dot value for the control law can be obtained.

If this formula is used to compute B-dot instead of using the buffer method, then the total time between sensor measurement and actuation will be decreased, since only one measurement is needed. Also, this formula allows us to consider estimated measurement-actuation delays by further extrapolation of B-dot. Additionally, it turns out to be optimal not only to compensate for these delays, but also to further extrapolate B-dot to get its value in the center of the actuation interval.

With these modifications, the boundary angular velocity of the algorithm implemented in MOVE-II could be increased to a theoretical limit of  $1200^{\circ}/s$ . This modified version of the detumbling algorithm was implemented into MOVE-IIb, with the possibility of changing delay estimations and actuation cycle timings from ground. Figure 17 shows the results of the modified controller test. In the figure it can be observed that the controller is stable at least up to a spin rate of approximately  $800^{\circ}/s$ .

### CONCLUSION

MOVE-II was operated in space for more than 6 months until now. In this time we could verify most of the subsystems and stabilize the satellite for regular operations. Even though we had some problems with the unexpectedly high spin rate of more than  $500^{\circ}/s$ , we could still find a way to detumble MOVE-II. We are now looking forward to the scientific operations phase of the satellite and performing

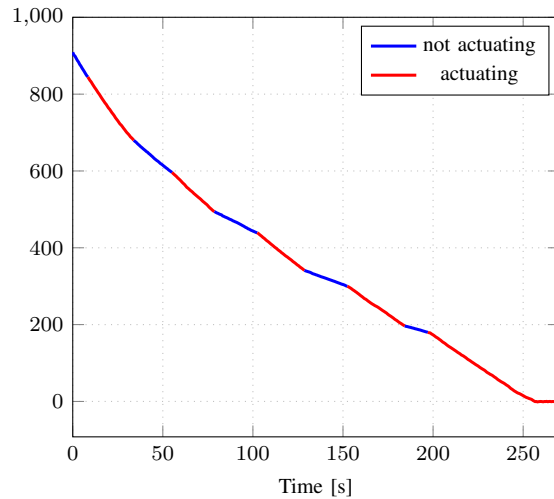


Figure 17: Observed Angular Velocity during a Helmholtz Cage Test using "Fast BDot" controller

regular measurements with our payload. At the same time we are awaiting the launch of MOVE-IIb with the improved wiring and the adapted controller. We hope that we were able to mitigate the issue that caused the satellite to spin itself up. At the same time we improved the capabilities of the system to cope with high spin rates to simplify operations of MOVE-IIb, if such high spin rates should be observed again.

### Acknowledgements

The authors acknowledge the funding of MOVE-II by the Federal Ministry of Economics and Energy, following a decision of the German Bundestag, via the German Aerospace Center (DLR) with funding grant number 50 RM 1509.

The authors acknowledge the support and launch opportunity provided by EXOLAUNCH for the MOVE-IIb satellite.

### References

- [1] Manuel Czech, Andreas Fleischner, and Ulrich Walter. "A First-MOVE in Satellite Development at the TU-München". In: *Small Satellite Missions for Earth Observation*. Springer, 2010, pp. 235–245.
- [2] M Langer et al. "Results and lessons learned from the CubeSat mission First-MOVE". In: *Small Satellite Missions for Earth Observation*. Springer, 2015.
- [3] M Langer and J Bouwmeester. "Reliability of CubeSats-Statistical Data, Developers' Beliefs and the Way Forward, AIAA". In: *USU Conference on Small Satellites*. 2016.
- [4] Martin Langer et al. "A reliability estimation tool for reducing infant mortality in Cubesat missions".

- In: *2017 IEEE Aerospace Conference*. IEEE. 2017, pp. 1–9.
- [5] D Messmann et al. “Advances in the Development of the Attitude Determination and Control System of the CubeSat MOVE-II”. In: *7th European Conference for Aeronautics and Space Sciences (EUCASS), Milan, Italy*. 2017.
  - [6] David Messmann et al. “Magnetic Attitude Control for the MOVE-II Mission”. In: *7th European Conference for Aeronautics and Space Sciences (EUCASS), Milan*. 2017.
  - [7] Consultative Committee for Space Data Systems (CCSDS). *TM Synchronization and Channel Coding*. CCSDS 131.0-B-2, Blue Book. Issue 2. Aug. 2011.
  - [8] Nicolas Appel, Sebastian Rückerl, and Martin Langer. “Nanolink: A Robust and Efficient Protocol for Small Satellite Radio Links”. In: *Small Satellite Systems and Services Symposium – 4S*. European Space Agency, 2016.
  - [9] Sebastian Rückerl et al. “Software-Defined Communication on the Nanosatellite MOVE-II”. In: *69th International Astronautical Congress*. 2018.
  - [10] M. Rutzinger et al. “On-orbit verification of space solar cells on the CubeSat MOVE-II”. In: 2016, pp. 2605–2609.
  - [11] Martin Buscher. *All Power to the ISS: First Results*. 2019. URL: <https://marconissta.com/2019/02/08/all-power-to-the-iss-first-results/> (visited on 06/07/2019).
  - [12] Zath-VHF. *SatNOGS Network - Observation 349561*. 2018. URL: <https://network.satnogs.org/observations/349561/> (visited on 06/09/2019).
  - [13] Jonis Kiesbye. “Hardware-in-the-Loop Verification of the Distributed, Magnetorquer-Based Attitude Determination & Control System of the CubeSat MOVE-II”. MA thesis. Institute of Astronautics, 2017.
  - [14] Libre Space Foundation. *SatNOGS Network - Observations (MOVE-II)*. 2019. URL: <https://network.satnogs.org/observations/?norad=43780> (visited on 06/09/2019).
  - [15] Dániel Nagy. “3-Channel Solar Array Simulator for CubeSat Power Budget Verification”. MA thesis. Institute of Astronautics, 2018.
  - [16] M. Langer et al. “MOVE-II The Munich Orbital Verification Experiment II”. In: 2017, pp. 441–459.
  - [17] M. Fleischhammer et al. “Interaction of cyclic ageing at high-rate and low temperatures and safety in lithium-ion batteries”. In: *Journal of Power Sources* 274 (2015), pp. 432–439.